RSC Advances

PAPER

View Article Online
View Journal | View Issue

Cite this: *RSC Adv.*, 2026, **16**, 1585

Organic–inorganic copper(II)-based perovskite: a low-toxic, highly stable light absorber for optoelectronic applications

Ines Khelifi,[a] Hanen Elgahami,[a] Imed Kammoun,[a] Nourah A. Alsobai,[b] Noweir Ahmad Alghamdi[c] and Abderrazek Oueslati *[a]

Organic–inorganic hybrid perovskites have emerged as promising next-generation materials for high-performance optoelectronic devices due to their structural tunability and versatile physical properties. In this work, bis(triethylammonium) chlorocuprate(II), $[(C_2H_5)_3NH]_2CuCl_4$ was successfully synthesized *via* a slow evaporation method. The crystal structure, morphology, and optical and electrical properties of $[(C_2H_5)_3NH]_2CuCl_4$ were systematically investigated using powder X-ray diffraction (PXRD), scanning electron microscopy coupled with energy-dispersive X-ray spectroscopy (SEM–EDS), Raman spectroscopy, UV-visible spectroscopy, and complex impedance spectroscopy. PXRD analysis reveals that the compound crystallizes in a monoclinic system with a centrosymmetric $P2_1/c$ space group at room temperature. SEM observations show uniformly distributed grains with an average size of approximately 17.5 μm, separated by well-defined grain boundaries, while EDS analysis confirms the expected elemental composition, indicating successful synthesis of the hybrid material. Raman spectroscopy confirms the coexistence of vibrational modes characteristic of both the organic and inorganic components. Optical absorption measurements recorded in the 200–800 nm range reveal a wide direct band gap of approximately 2.36 ± 0.004 eV, characteristic of semiconducting hybrid perovskites. Electrical investigations demonstrate that the AC conductivity follows Jonscher's universal power law, indicating a thermally activated charge transport process over the investigated frequency range. Moreover, the temperature dependence of the frequency exponent *s* reveals that the correlated barrier hopping (CBH) model governs the electrical conduction mechanism in the studied material. Furthermore, complex modulus analysis provides additional insight into the relaxation behavior and the dominant electrical transport mechanisms.

Received 5th November 2025
Accepted 26th December 2025

DOI: 10.1039/d5ra08521g

rsc.li/rsc-advances

1. Introduction

Organic–inorganic hybrid perovskites (OIHPs) have attracted considerable attention in recent years due to their outstanding performance in optoelectronic applications, including light-emitting diodes, photodetectors, radiation detectors and solar cells.[1–9] Their remarkable success originates from the synergistic combination of organic and inorganic components, which enables exceptional tunability of structural, optical, and electronic properties. Recent reviews and experimental studies have emphasized that compositional flexibility and reduced dimensionality play a key role in optimizing charge transport, optical absorption, and environmental stability in hybrid perovskite systems.[10–12] A distinctive advantage of OIHPs lies in their ability to adopt various structural dimensionalities, ranging from zero-dimensional (0D) to one-dimensional (1D), two-dimensional (2D), and three-dimensional (3D) architectures, depending on the nature of the organic cation and the inorganic framework.[13–15] In particular, low-dimensional hybrid perovskites have emerged as promising alternatives to conventional 3D structures, as they often exhibit enhanced structural stability and tunable electronic behavior. In this context, hybrid compounds composed of metal halide frameworks coordinated with organic molecules offer attractive opportunities for discovering novel physical properties and multifunctional materials.[16–18] Among the different structural families, layered perovskite-like compounds with the general formula $A_2M^{2+}X_4$ have received significant attention. In these materials, A represents a protonated organic cation (*e.g.*, methylammonium or ethylammonium), M^{2+} is a divalent metal ion (such as Cu^{2+}, Zn^{2+}, or Mn^{2+}), and *X* is a halide anion (Cl^-, Br^-, or I^-).[19–21] The alternating stacking of organic and inorganic layers, held

[a]*Laboratory of Spectroscopic Characterization and Optical Materials, Faculty of Sciences, University of Sfax, B.P. 1171, Sfax 3000, Tunisia. E-mail: oueslatiabderrazek@yahoo.fr*

[b]*Department of Physics, College of Science, Taif University, P.O. Box 11099, Taif, 21944, Saudi Arabia*

[c]*Departement of Physics, Faculty of Science, Al-Baha University, Alaqiq, 65779, Saudi Arabia*

together mainly by van der Waals interactions and hydrogen bonding, leads to a two-dimensional perovskite structure. This layered arrangement has been shown to strongly influence exciton confinement, dielectric response, and charge transport properties, making 2D OIHPs particularly attractive for optoelectronic applications.[22] Within this family, copper-based hybrid perovskites stand out as especially interesting candidates. The presence of Cu^{2+} ions with a $3d^9$ electronic configuration gives rise to Jahn–Teller distortions, resulting in flexible coordination environments and enhanced structural tunability.[23] Moreover, copper is a non-toxic and earth-abundant element, addressing the major environmental and health concerns associated with lead- and cadmium-based perovskites. Cu-based hybrid halides have also demonstrated strong optical absorption across a wide spectral range, making them promising materials for lead-free optoelectronic devices.[24] Despite the rapid progress in perovskite solar cells and related technologies, several critical challenges remain, notably the toxicity of Pb-, Cd-, and Hg-based perovskites and the poor stability of some lead-free alternatives such as Sn- and Bi-based compounds under light, moisture, heat, and mechanical stress.[25] Recent studies have therefore highlighted the urgent need to develop non-toxic, stable perovskite-like materials with suitable electronic and optical properties for sustainable optoelectronic applications.[10–12] In this regard, layered Cu(II)-based hybrid perovskites have been revisited as promising Pb-free semiconductors combining stability, tunability, and functional performance.[26] Based on these considerations, the present work focuses on the synthesis and comprehensive characterization of the Cu-based perovskite-like hybrid halide $[(C_2H_5)_3NH]_2CuCl_4$. Previous studies by Ozga *et al*. reported that this compound crystallizes in a two-dimensional layered perovskite structure.[27,28] However, a detailed correlation between its crystal structure, microstructure, vibrational

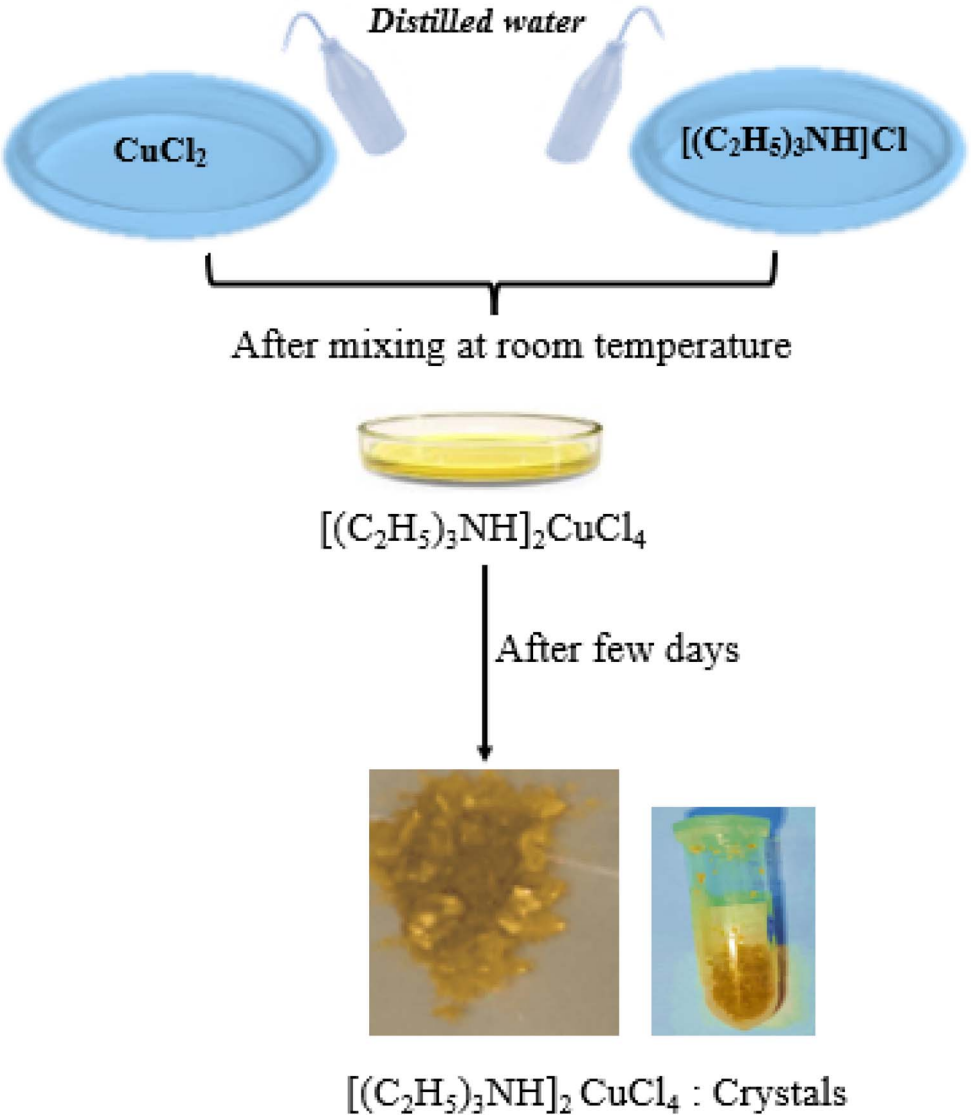

Fig. 1 Synthesis of $[(C_2H_5)_3NH]_2CuCl_4$ single crystals.

features, optical absorption, and electrical transport properties remains limited. In this study, $[(C_2H_5)_3NH]_2CuCl_4$ was synthesized and systematically investigated using powder X-ray diffraction (PXRD) to confirm phase purity and crystallinity. Scanning electron microscopy (SEM) coupled with energy-dispersive X-ray spectroscopy (EDS) was used to examine surface morphology and elemental composition, while Raman spectroscopy was employed to analyze vibrational modes and bonding characteristics. UV-visible spectroscopy was used to evaluate the optical absorption properties and band gap, which are crucial parameters for optoelectronic applications and impedance spectroscopy was carried out to elucidate the electrical and dielectric behavior.

2. Experimental

2.1. Synthesis of $[(C_2H_5)_3NH]_2CuCl_4$

All chemical reagents were used as received from Sigma-Aldrich without further purification. Single crystals of $[(C_2H_5)_3NH]_2CuCl_4$ were grown using a slow evaporation method at ambient temperature. Triethylammonium chloride $[(C_2H_5)_3NH]Cl$ (Fluka, purity 98%, 1.487 mmol) and copper(II) chloride $CuCl_2$ were dissolved in a small amount of distilled water and magnetically stirred to ensure a homogeneous solution. The resulting solution was then left to evaporate slowly at room temperature (approximately 28 °C). Yellow, transparent single crystals began to form after several days (see Fig. 1). The reaction proceeds according to eqn (1).

$$2[(C_2H_5)_3NH]Cl + CuCl_2 \xrightarrow{H_2O} [(C_2H_5)_3NH]_2CuCl_4 \quad (1)$$

2.2. Characterization

To ensure the phase purity and homogeneity of $[(C_2H_5)_3NH]_2CuCl_4$, high precession powder X-ray diffraction (PXRD) measurement was carried out at room temperature. Data were collected using a Bruker D8 diffractometer with Cu Kα radiation ($\lambda = 1.54056$ Å) over a Bragg's angle of $5° \leq 2\theta \leq 50°$.

To visualize and quantify the intermolecular interactions within the crystal structure, Hirshfeld surface (HS) analysis was performed using the CrystalExplorer software,[29] based on the crystallographic information file (CIF).

On the other hand, Raman spectroscopy was employed to confirm the presence of both organic and inorganic groups, as well as to identify their vibrational modes. The Raman spectrum was recorded using a Horiba HR 800 micro-Raman spectrometer equipped with a helium-ion laser, operating with a red exciting ray ($\lambda = 633$ nm) in the frequency range 50–3500 cm^{-1}.

Raman spectroscopy was employed to confirm the coexistence of organic and inorganic components and to identify their vibrational modes. The Raman spectrum was recorded using a Horiba HR800 micro-Raman spectrometer equipped with a He–Ne laser ($\lambda = 633$ nm), operating in the spectral range of 50–3500 cm^{-1}.

The surface morphology and elemental composition were examined using a scanning electron microscope (SEM, JEOL JSM-6510LV) coupled with energy-dispersive X-ray spectroscopy (EDS). The ImageJ software was used to analyze SEM micrographs, evaluate particle size distributions, and generate corresponding histograms.

Optical measurements were carried out using a Shimadzu UV-3101 PC UV-is spectrophotometer over the wavelength range of 200–800 nm, employing a xenon lamp as the light source. A spectral resolution of 2 nm was used to ensure accurate acquisition of absorbance and reflectance spectra.

Electrical measurements were performed using a Solartron SI 1260 impedance analyzer coupled with a Solartron 1296 dielectric interface. Temperature control was achieved using a Linkam LTS420 system. Impedance data were collected over a frequency range of 10^2–10^6 Hz and a temperature range of 273–313 K, with an applied AC voltage of 0.5 V. The measurements were carried out on a pellet with a diameter of 8 mm and a thickness of 1.1 mm.

3. Results and discussion

3.1. X-ray diffraction

Rietveld refinement of the bis(triethylammonium) chlorocuprate(II) compound was performed using the Fullprof software package.[30] The calculated diffraction pattern shows excellent agreement with the experimental powder X-ray diffraction (PXRD) data, as illustrated in Fig. 2. The quality of the refinement is confirmed by the reliability factors ($R_p = 12.6$, $R_{wp} = 18.0$, $R_{exp} = 6.94$, and $\chi^2 = 6.76$), indicating a satisfactory structural model and good convergence. The PXRD pattern was successfully indexed in the centrosymmetric monoclinic space group $P2_1/c$. The refined lattice parameters are: $a = 12.783$ Å, $b = 12.914$ Å, $c = 12.113$ Å, and $\beta = 98.02°$, in good agreement with previously reported layered chlorocuprate perovskite structures.

The quality of the refinement is confirmed by the reliability factors ($R_p = 12.6$, $R_{wp} = 18.0$, $R_{exp} = 6.94$, and $\chi^2 = 6.76$), indicating a satisfactory structural model and good

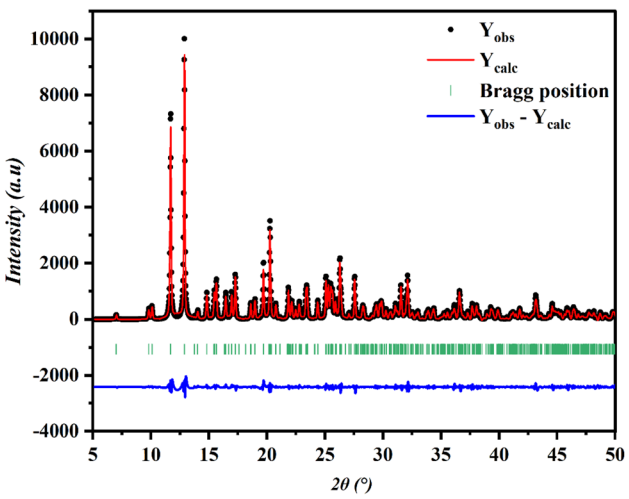

Fig. 2 Powder X-ray diffraction pattern and Rietveld refinement of $[(C_2H_5)_3NH]_2CuCl_4$.

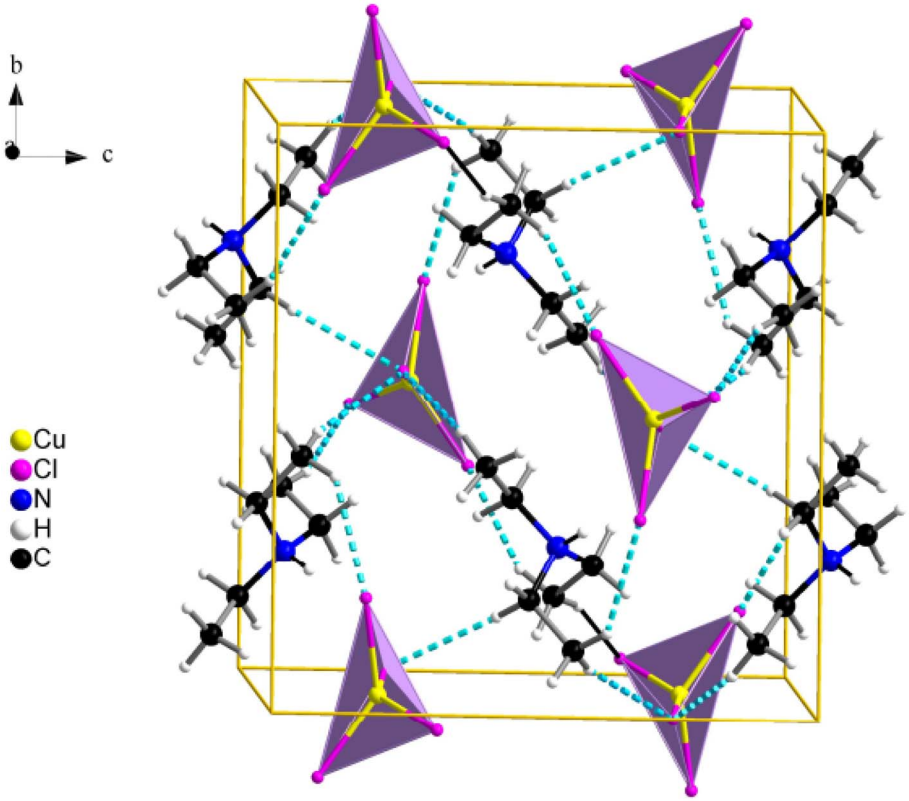

Fig. 3 Crystal packing arrangement of $[(C_2H_5)_3NH]_2CuCl_4$ compound.

convergence. The PXRD pattern was successfully indexed in the centrosymmetric monoclinic space group $P2_1/c$. The refined lattice parameters are $a = 12.783$ Å, $b = 12.914$ Å, $c = 12.113$ Å, and $\beta = 98.02°$. These results are consistent with those obtained from single-crystal X-ray diffraction reported in the literature, thereby confirming the phase purity of the synthesized compound.[31] The average crystallite size was estimated from the XRD peak broadening using the Debye–Scherrer equation.[32]

$$D = \frac{K\lambda}{\beta \cos\theta} \quad (2)$$

Where D is the crystallite size, K is the shape factor (≈ 0.9), λ is the X-ray wavelength ($\lambda = 1.54$ Å), β is the full width at half maximum (FWHM) of the most intense diffraction peak corresponding to the (hkl) plane, and θ is the Bragg angle (in radians). The calculated crystallite size is approximately 8 nm, indicating a nanocrystalline nature.

Notably, the Rietveld-refined nanometric crystallite size contrasts with the micrometer-sized grains observed in SEM images, suggesting that the material consists of nanoscale crystallites aggregated into larger grains. This multiscale structural organization is commonly observed in hybrid perovskite materials and has been reported in similar systems.[33] Fig. 3 shows the crystal structure of $[(C_2H_5)_3NH]_2CuCl_4$. As shown in the figure, the structure consists of two crystallographically independent triethylammonium cations $[(C_2H_5)_3NH]^+$ and a single $[CuCl_4]^{2-}$ anion. Each Cu(II) center is coordinated by four chloride ions, forming a distorted tetrahedral geometry around the copper atom. The Cu–Cl bond lengths range from 2.2368(5) to 2.2487(5) Å, while the Cl–Cu–Cl bond angles vary between 96.093(2)° and 139.01(2)°. The crystal structure can be described as an alternating arrangement of organic and inorganic layers along the [101] direction. The cohesion between the organic and inorganic components is ensured by C–H···Cl hydrogen bonds.

3.2. Hirshfeld surface analysis

The Hirshfeld surface was mapped using the d_{norm} descriptor, which incorporates two parameters: d_e and d_i. Here, d_e represents the distance from a point on the surface to the nearest external atom, while d_i corresponds to the distance to the nearest internal atom.[34] The d_{norm}, d_e and d_i surfaces of the title compound are shown in Fig. 4. The d_{norm} parameter is a normalized contact distance that reflects the proximity of intermolecular contacts in specific regions of the Hirshfeld surface, enabling the identification of hydrogen bonds and other close contacts. Red circular depressions on the d_{norm} surface typically correspond to strong hydrogen bonding interactions, whereas weaker interactions appear as smaller regions in lighter shades. Specifically, red regions indicate close contacts ($d_{norm} < 0$), blue regions represent longer contacts ($d_{norm} > 0$), and white regions correspond to contacts at van der Waals separation ($d_{norm} \approx 0$).

In Fig. 4, the d_{norm} color scale for $[(C_2H_5)_3NH]_2CuCl_4$ ranges from −0.5453 to 1.2370 Å, with the dominant intermolecular

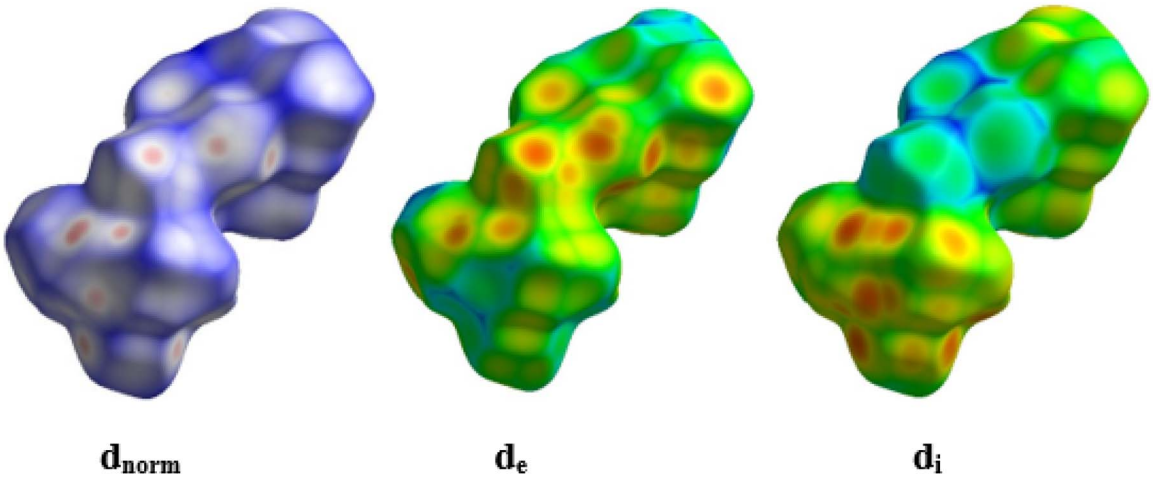

Fig. 4 The Hirshfeld surface of $[(C_2H_5)_3NH]_2CuC_{l4}$ mapped with d_{norm}, d_e and d_i.

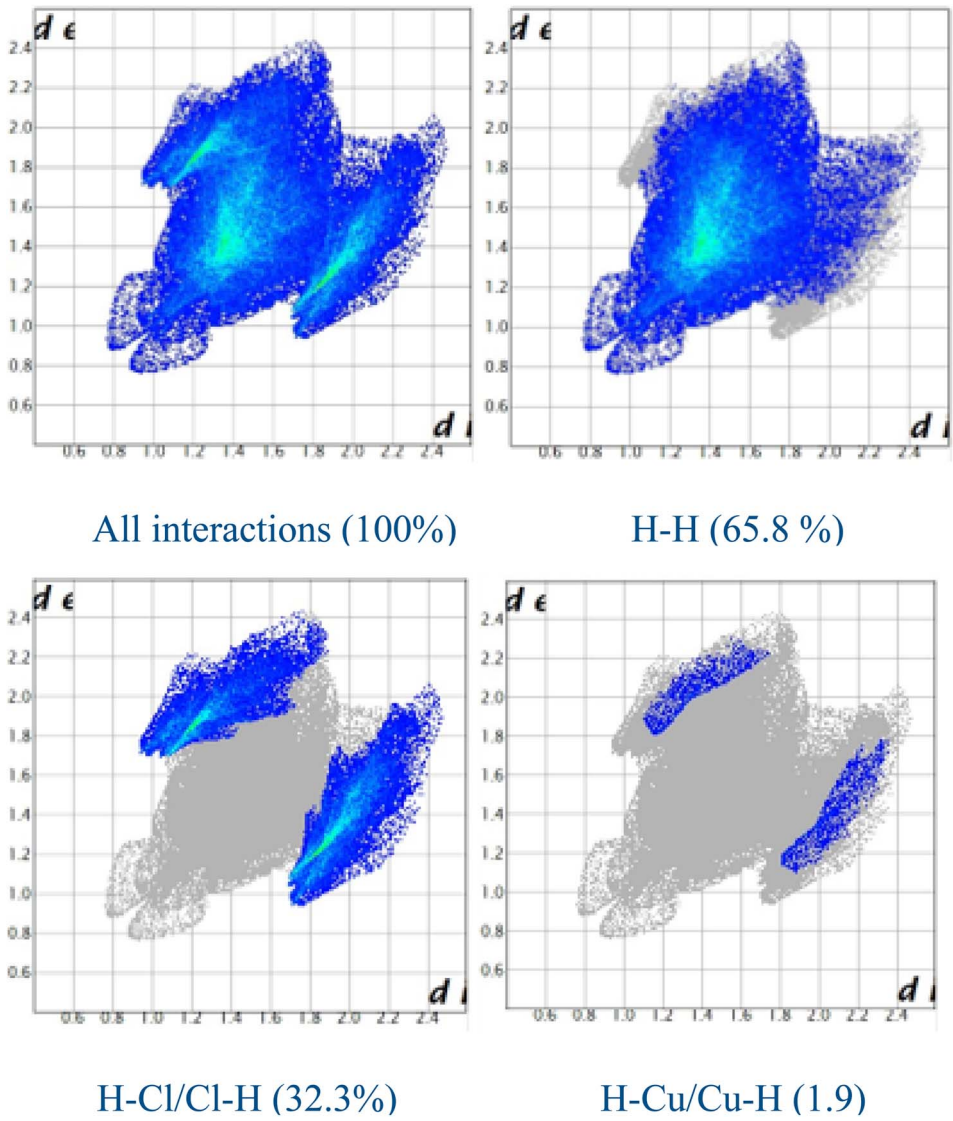

Fig. 5 2D fingerprint plots corresponding to the different intermolecular contacts for the title compound.

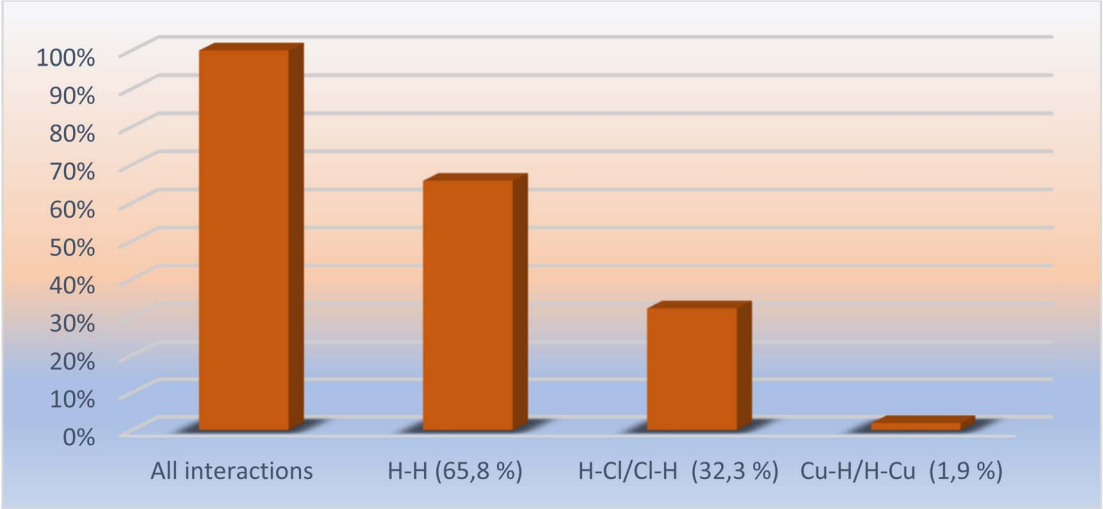

Fig. 6 Histogram showing the relative contributions of various intermolecular contacts to the HS area.

interaction being Cl···H/H···Cl contacts. Hirshfeld surface analysis also generates two-dimensional (2D) fingerprint plots that quantitatively identify different types of molecular interactions, including intra- and intermolecular contacts, and their relative contributions to the Hirshfeld surface area. As shown in Fig. 5, the dominant interactions in the crystal packing of $[(C_2H_5)_3NH]_2CuCl_4$ are H···H (65.8%) and Cl···H/H···Cl (32.3%) contacts, which together account for 98.1% of all intermolecular interactions. The Cl···H/H···Cl interactions arise from C–H···Cl hydrogen bonds. Symmetrical spikes observed in the 2D fingerprint plot further confirm Cl···H electrostatic attractions between positively polarized hydrogen atoms H^+ and chloride anions Cl^-. In contrast, H···H interactions reflect the close spatial proximity of hydrogen atoms within the structure. The relative contributions of the various close intermolecular contacts are summarized in Fig. 6.

3.3. SEM-EDX analysis

Scanning electron microscopy (SEM) analysis of the bis(triethylammonium) chlorocuprate(II) compound was carried out on crystalline samples to examine their surface morphology. The corresponding micrograph is presented in Fig. 7a. The SEM image reveals particles with similar morphologies but varying sizes. The corresponding particle size distribution histogram is shown in Fig. 7b. The average grain size is approximately 17.5 μm, indicating the successful synthesis of microparticles.

Energy-dispersive X-ray spectroscopy (EDX) was performed to verify the elemental composition of the synthesized material. The EDX spectrum, shown in Fig. 7c, exhibits distinct characteristic peaks corresponding to copper (Cu), chlorine (Cl) and carbon (C), which are the non-hydrogen constituent elements of the compound. No impurity peaks were observed, confirming the high purity of $[(C_2H_5)_3NH]_2CuCl_4$ compound.

3.4. Raman vibrational study

Raman spectroscopy was employed to investigate the vibrational modes of both the organic and inorganic components of the bis(triethylammonium) chlorocuprate(II) compound. The Raman spectrum, recorded at room temperature over the wavenumber range from 50 cm^{-1} to 3200 cm^{-1}, is shown in Fig. 8, and the corresponding vibrational band assignments are summarized in Table 1. All assignments were made by comparison with Raman spectra reported in previous studies of structurally related compounds.[35–38] The Raman bands observed below 400 cm^{-1} are attributed to the internal vibrational modes of the anionic $[CuCl_4]^{2-}$ group. The intense band observed at 78 cm^{-1} is assigned to the symmetric deformation mode, δ_s($CuCl_4$), while the asymmetric deformation mode, δ_{as} ($CuCl_4$), appears at 100 cm^{-1}. The symmetric stretching vibration, υ_s($CuCl_4$), is detected at 278 cm^{-1}, whereas the asymmetric stretching vibration, υ_{as} ($CuCl_4$), is observed at 310 cm^{-1}. The cationic $[(C_2H_5)_3NH]^+$ group exhibits several vibrational modes in the spectral range from 410 cm^{-1} to 2984 cm^{-1}. The band observed around 410 cm^{-1} is attributed to the symmetric deformation mode, δ_s(C–N–C). Vibrational modes of the CH_3 groups, including stretching, deformation and rocking are observed at 734, 1058, 1450, and 2984 cm^{-1}. In contrast, CH_2 group vibrations, such as twisting, torsion and stretching modes, appear at approximately 1312, 1342, 2886 and 2943 cm^{-1}, respectively. In addition, the skeletal deformation mode (C–C–N) is observed at 1209 cm^{-1}, the symmetric stretching vibration υ_s(C–N) appears near 892 cm^{-1} and the N–H stretching vibration is detected around 2746 cm^{-1}.

3.5. UV-visible measurement

3.5.1. Absorbance and reflectance. The absorbance and reflectance spectra of the $[(C_2H_5)_3NH]_2CuCl_4$ compound, recorded at room temperature, are presented in Fig. 9. The absorbance spectrum exhibits four distinct peaks at 280 nm, 346 nm, 390 nm, and 468 nm. The strong absorption observed in this region can be attributed to electronic transitions from the valence band to the conduction band. This behavior is consistent with previous studies on $[CuCl_4]^{2-}$ complexes[39,40] and indicates the presence of a characteristic band gap in the

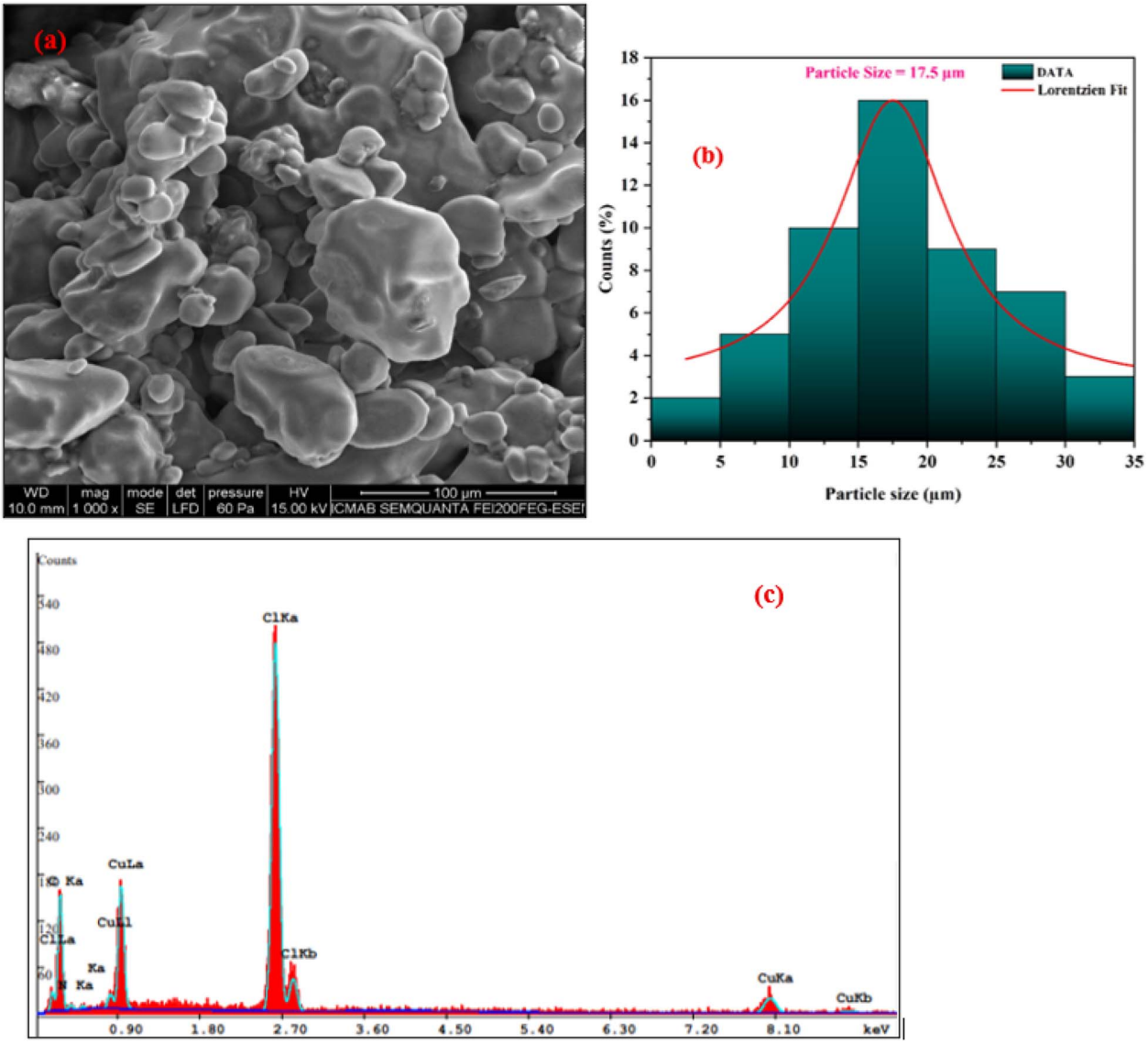

Fig. 7 SEM micrograph (a), Size distribution histogram (b) and EDX analysis (c) of $[(C_2H_5)_3NH]_2CuC_{l4}$.

material. Moreover, the title compound exhibits high reflectance in the visible and near-infrared (NIR) regions, which is a desirable property for optoelectronic applications such as light-emitting diodes (LEDs) and solar cells.

3.5.2. Gap energy. The band gap energy of bis(triethylammonium) chlorocuprate(II) was determined using the Kubelka–Munk function, as described by the following relation:[41]

$$(F(R) \times h\upsilon)^{1/n} = A(h\upsilon - E_g) \quad (3)$$

$F(R) = \dfrac{(1-R)^2}{2R}$, is the Kubelka–Munk function and R represents reflectance. The parameter n is the transition index, taking the value $n = \dfrac{1}{2}$ for allowed direct transitions and $n = 2$ for allowed indirect transitions, E_g denotes the optical band gap, A is a constant related to the transition probability (Tauc parameter)[42,43] and $h\upsilon$ is the photon energy of the incident light.

Fig. 10 depicts the variation $(F(R) \times h\upsilon)^{1/n}$ as a function of the photon energy $E = h\upsilon$ with $n = \dfrac{1}{2}$ and $n = 2$ corresponding to direct and indirect band gap transitions, respectively. From the extrapolation of the linear regions, the band gap energies were determined to be $E_g = 2.36 \pm 0.004$ eV for the direct transition and $E_g = 2.17$ eV $E_g = 2.17 \pm 0.003$ eV for the indirect transition. To determine the nature of the electronic transition (direct or indirect band gap) in $[(C_2H_5)_3NH]_2CuCl_4$, the first derivative of the reflectance spectrum, expressed as $[(1/R) \times (dR/d\lambda)]$, was analyzed. This method allows the estimation of the optical band gap based on the positions of inflection points in the reflectance spectrum.[44] Fig. 11 shows in the amplitude of this derivative as a function of wavelength.

Using the relationship between the band gap energy and wavelength, $E_g = 1240/\lambda$ (nm), the optical band gap was

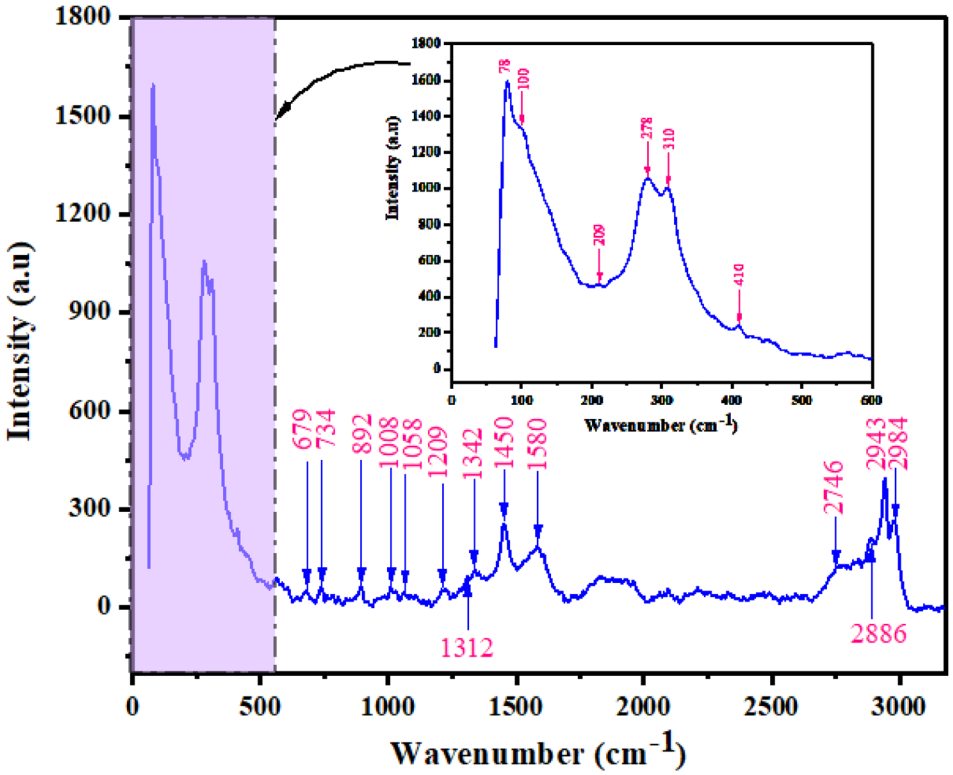

Fig. 8 Raman spectrum of $[(C_2H_5)_3NH]_2CuCl_4$ compound at room temperature.

Table 1 Assignments of most important observed bands in Raman spectrum of $[(C_2H_5)_3NH]_2CuCl_4$ at room temperature[a]

Raman wavenumber (cm^{-1})	Assignments
78	δ_s ($CuCl_4$)
100	δ_{as} ($CuCl_4$)
209	—
278	ν_s ($CuCl_4$)
310	ν_{as} ($CuCl_4$)
410	δ_s (C–N–C)
679	—
734	ρ (CH_3)
892	ν_s (C–N)
1008	ν (C–C)
1058	ρ (CH_3)
1209	(CCN) skeleton
1312	τ (CH_2)
1342	ω (CH_2)
1450	δ_{as} (CH_3)
1580	—
2746	ν (NH)
2886	ν (CH_2)
2943	ν_s (CH_2)
2984	ν_{as} (CH_3)

[a] ν_s: symmetric stretching, ν_{as}: asymmetric stretching; δ_s: symmetric deformation; δ_{as}: asymmetric deformation; τ: twisting; ρ: rocking, ω: torsion.

estimated to be approximately 2.37 ± 0.004 eV, corresponding to a prominent peak at 521.50 nm. On the basis of the band gap value obtained from the $(1/R)$ *$(dR/d\lambda)$ *versus* λ plot, the optical absorption process is confirmed to be of a direct transition nature. The compound exhibits significant light absorption in the visible region, extending over the wavelength range of 400–800 nm, which highlights the semiconducting behavior of the studied Cu(II) complex. This result is consistent with previously reported band gap values for similar hybrid materials based on $[CuCl_4]^{2-}$ units, such as: $[CH_3NH_3]_2CuCl_4$ (E_g = 2.63 eV),[45], $[C_6H_9N_2]_2CuCl_4$ (E_g = 2.47 eV),[46], $[C_4H_{14}N_2]_2CuCl_4$ (E_g = 2.47 eV).[47]

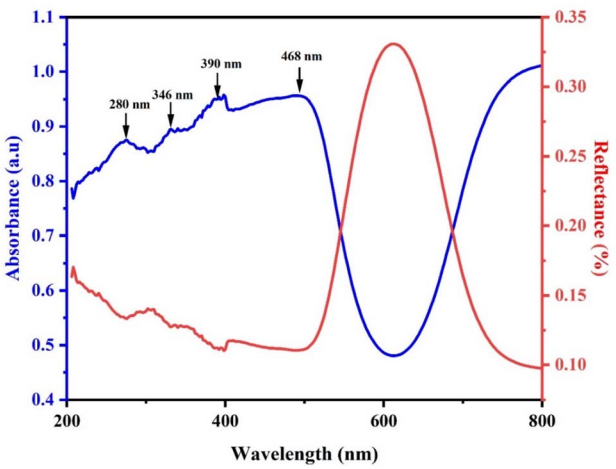

Fig. 9 Room temperature UV-vis absorption and diffuse reflectance spectra.

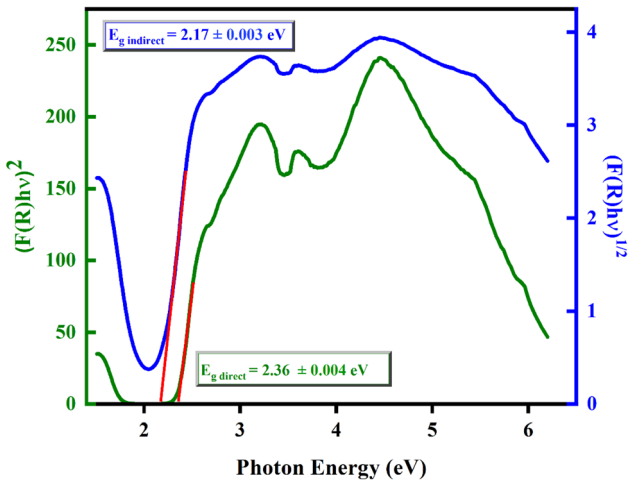

Fig. 10 Kubelka–Munk plots for direct and indirect band gap of $[(C_2H_5)_3NH]_2CuCl_4$.

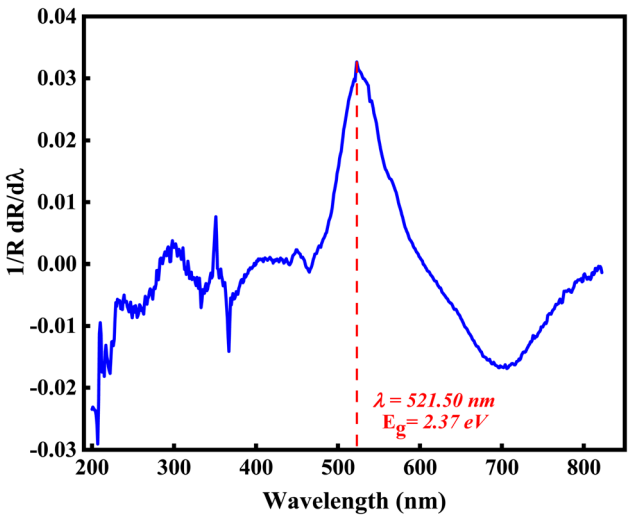

Fig. 11 $dR/Rd\lambda$ as a function of wavelength (λ).

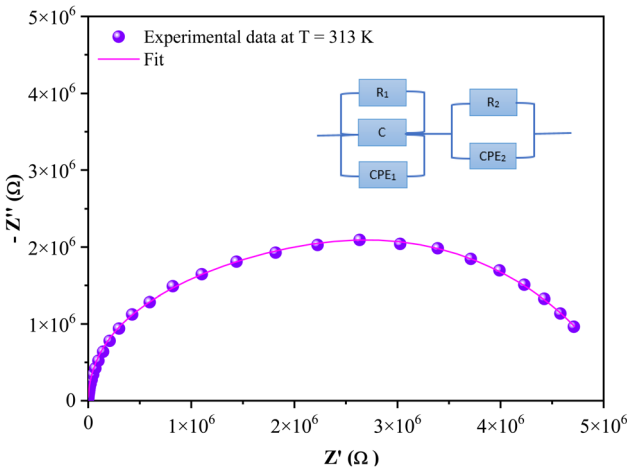

Fig. 12 Nyquist plot ($-Z''$) *vs.* (Z') at $T = 313$ K, inset equivalent circuit.

3.6. Complex impedance analysis

Complex impedance spectroscopy is a powerful technique for investigating the electrical properties of materials. It enables clear differentiation between various transport phenomena and provides insights into the relative contributions of different mechanisms involved in the overall conduction process.[48]

3.6.1. Nyquist plots. The Nyquist plot ($-Z''$ *vs.* Z') of the title compound, recorded at 313 K, is presented in Fig. 12. The plot exhibits two well-defined semicircles, which can be attributed to the electrical responses of the grains and grain boundaries, respectively.[49] Furthermore, the decrease in the diameters of these semicircles with increasing temperature indicates a reduction in the material's resistance, characteristic of negative temperature coefficient of resistance (NTCR) behavior.[50,51] This trend reflects a thermally activated conduction mechanism, confirming the semiconducting nature of the $[(C_2H_5)_3NH]_2CuCl_4$ material.

Fig. 13a illustrates the variation of the real part of the impedance (Z') with frequency at different temperatures [273 K–313 K]. At low frequencies, Z' increases as the temperature rises from 273 K to 293 K. Above 293 K, Z' decreases with increasing temperature, which can be attributed to the reduction of trapped charge density and the thermal activation of charge carrier mobility.[52] Additionally, at high frequencies (>10^5 Hz), the Z' values converge, indicating that the charge carriers have acquired sufficient energy to overcome the potential barriers.[53] The variation of the imaginary part of the impedance ($-Z''$) as a function of the angular frequency (ω) shown in Fig. 13b, exhibits a well-defined relaxation peak at each temperature. As the temperature increases, the maximum of Z'' shifts toward higher frequencies and decreases in magnitude. This behavior reflects a thermally activated relaxation process characterized by shorter relaxation times at higher temperatures, due to the enhanced mobility of charge carriers.[54,55] Overall, these observations confirm the semiconducting nature of the material.

3.6.2. AC electrical conductivity. AC conductivity (σ_{AC}) is a fundamental property that reflects the electrical dynamics of a material, encompassing parameters such as conductivity, capacitance, and loss factor. It also provides insight into the conduction mechanism and how these properties vary with temperature and frequency. Fig. 14 shows AC conductivity spectra recorded over the temperature range 273–313 K revealing two distinct regions. At low frequencies, the conductivity remains nearly constant, indicating a region dominated by direct current (DC) conduction, where mobile charge carriers respond efficiently to the applied electric field. At high frequencies, a dispersion region appears, corresponding to AC conduction, where the electrical response becomes more complex due to the involvement of trapped charges. Furthermore, at a constant frequency, σ_{AC} increases with temperature, consistent with a carrier hopping process, indicating that the conduction mechanism is predominantly thermally activated.[56,57] The phenomenon of conductivity dispersion is generally described by the following equation:[41]

$$\sigma_{AC}(\omega) = \frac{\sigma_s}{1+\tau^2\omega^2} + \frac{\sigma_\infty \tau^2\omega^2}{1+\tau^2\omega^2} + A\omega^s \quad (4)$$

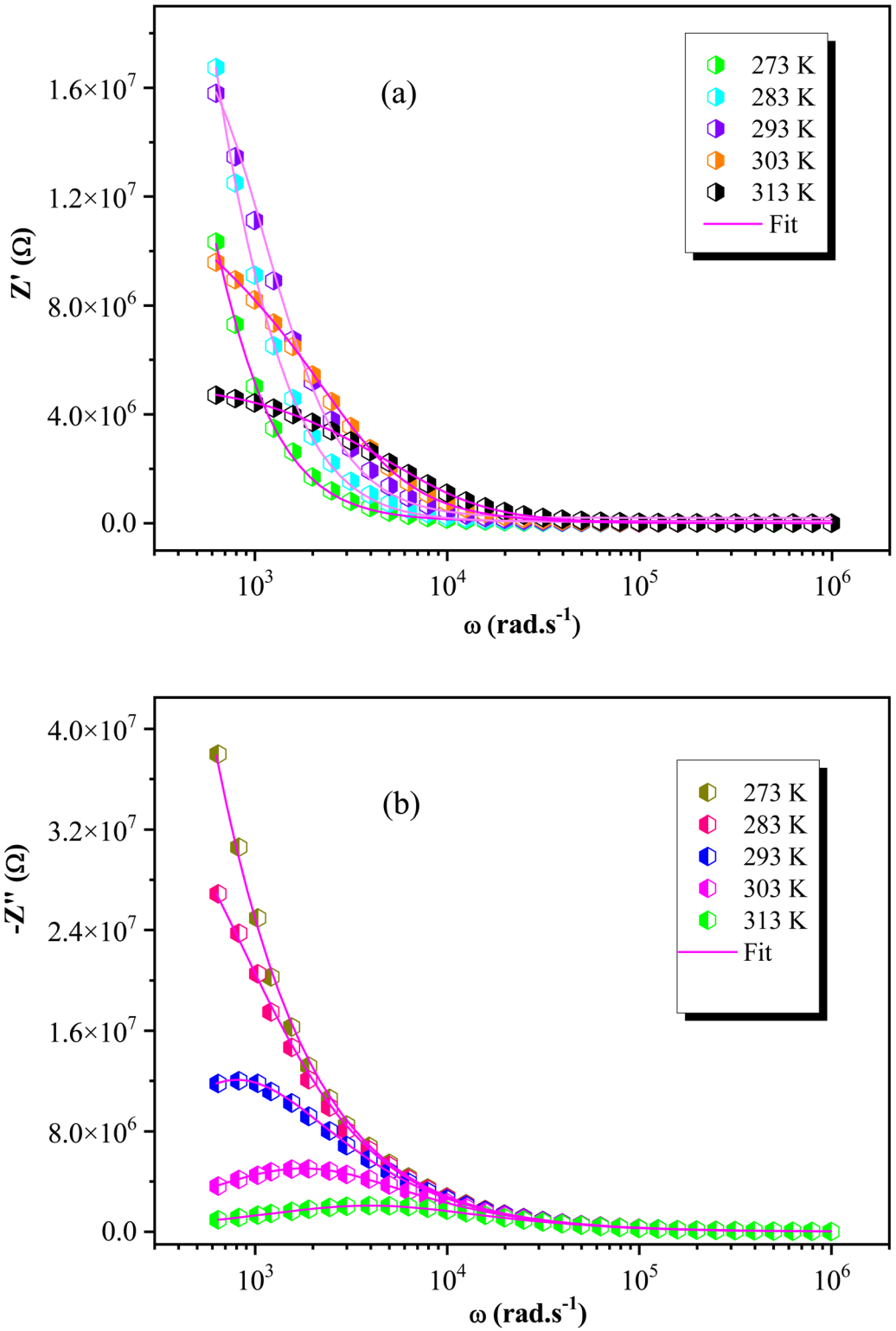

Fig. 13 Variations of real (Z′) (a) and imaginary (−Z″) (b) parts of impedance as a function of frequency at several temperatures.

Here, σ_s denotes the conductivity in the low frequency region, while σ_∞ corresponds to the estimated conductivity at high frequencies, τ represents the relaxation time, A is a temperature-dependent constant and $\omega = 2\pi f$ is the angular frequency. The DC conductivity data, presented as a plot of ln (σ_{DC} T) *vs.* 1000/T^{-1} *versus* 1000/T^{-1} over the temperature range 273–313 K (Fig. 15a), exhibits Arrhenius-type behavior, which is described by the following equation:[58]

$$\sigma_{DC} = \sigma_0 \exp\left(-\frac{E_a}{K_B T}\right) \quad (5)$$

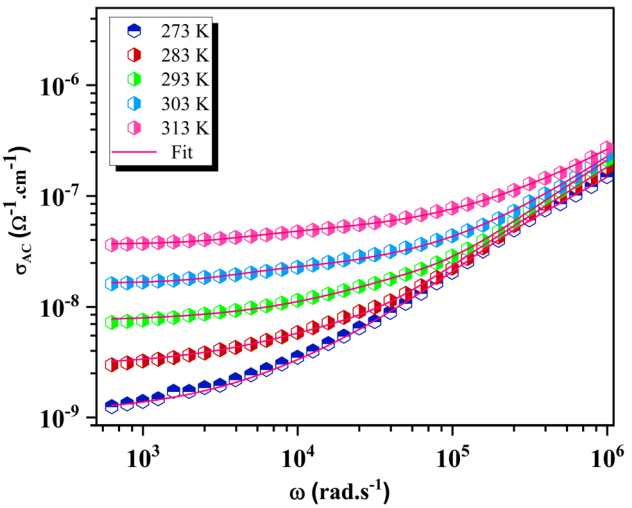

Fig. 14 Angular frequency dependence of the AC conductivity at various temperatures.

where σ_0 is the pre-exponential factor, E_a is the activation energy and K_B is the Boltzmann constant. From the plotted graph, it is evident that the DC conductivity increases with increasing temperature, confirming the thermally activated nature of the conduction mechanism. Linear fitting of the ln (σ_{DC}.T) *versus* 1000/T^{-1} data yielded an activation energy of approximately 0.65 eV over the temperature range 273–313 K. This value indicates that the conduction is governed by a thermally activated hopping process.

Fig. 15b presents the variation of the frequency exponent, s, as a function of temperature for $[(C_2H_5)_3NH]_2CuCl_4$. The gradual decrease in s with increasing temperature indicates an improvement in the electrical conductivity of the material. This behavior suggests a change in the conduction mechanism, which can be interpreted using several theoretical models based on the temperature dependence of s. Several microscopic models have been developed to better understand conduction mechanisms in materials, including Quantum Mechanical Tunneling (QMT), Correlated Barrier Hopping (CBH), Non-overlapping Small Polaron Tunneling (NSPT), and Overlapping Large Polaron Tunneling (OLPT).[59–61] For the present compound, the observed decrease of s with temperature strongly suggests that the CBH model is the most appropriate. In this model, charge carriers move *via* successive hops between localized sites separated by potential barriers. The frequency exponent s is described by the following expression:[62]

$$s = 1 - \frac{6k_B\,T}{W_M + k_B\,T\ln(\omega\tau_0)} \quad (6)$$

Here, τ_0 is the characteristic relaxation time, W_M is the self-trapping energy required for a charge carrier to hop between localized sites, k_B is the Boltzmann constant and T is the absolute temperature. If $W_M >> k_BT\ln(\omega\tau_0)$, relation (4) can be simplified as follows:

$$s = 1 - \frac{6k_B\,T}{W_M} \quad (7)$$

3.6.3. Dielectric modulus. The analysis of electrical properties is based on the complex modulus formalism, which is particularly well-suited for emphasizing the bulk response of the crystal sample and for revealing phenomena such as electrode polarization and conductivity relaxation times.[63] The total complex modulus M^* is defined by the following equation:[64]

$$M^* = M' + M'' = i\omega C_0 Z^* \quad (8)$$

Here, M' and M'' are the real and imaginary parts of the complex modulus, respectively, C_0 represents the vacuum capacitance and Z^* is the complex impedance.

The frequency dependence of the imaginary part, M'', measured at different temperatures, is shown in Fig. 16a. The plot exhibits distinct relaxation peaks, which systematically shift toward higher frequencies as the temperature increases. This behavior indicates that the relaxation process is thermally activated and associated with enhanced charge carrier mobility.

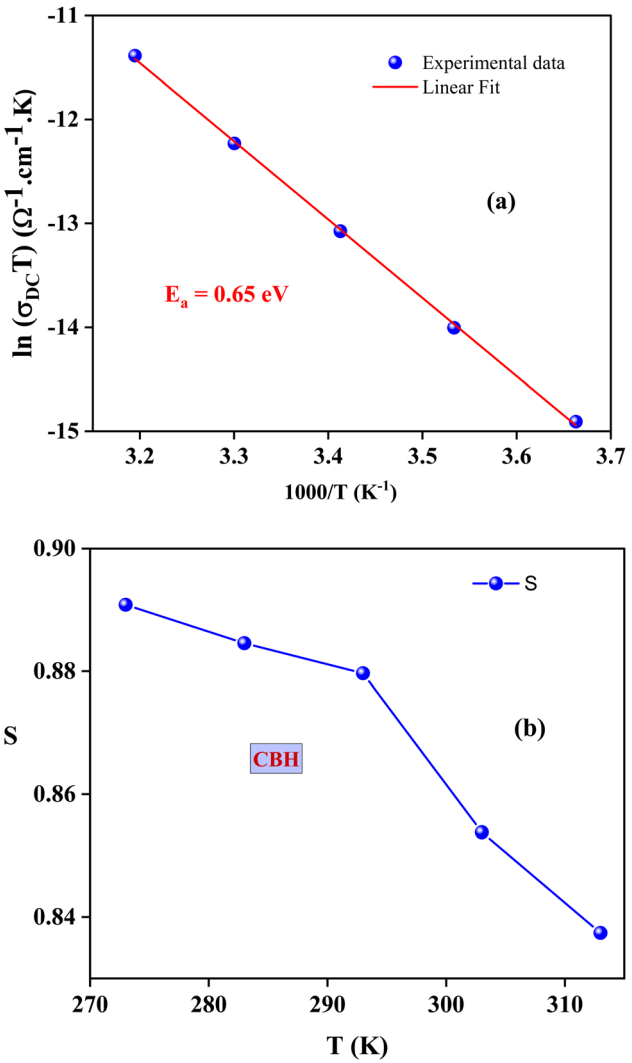

Fig. 15 (a) Variations of ln(σ_{DC} T) *versus* (1000/T^{-1}) and the exponent (s) as a function of the temperature (b).

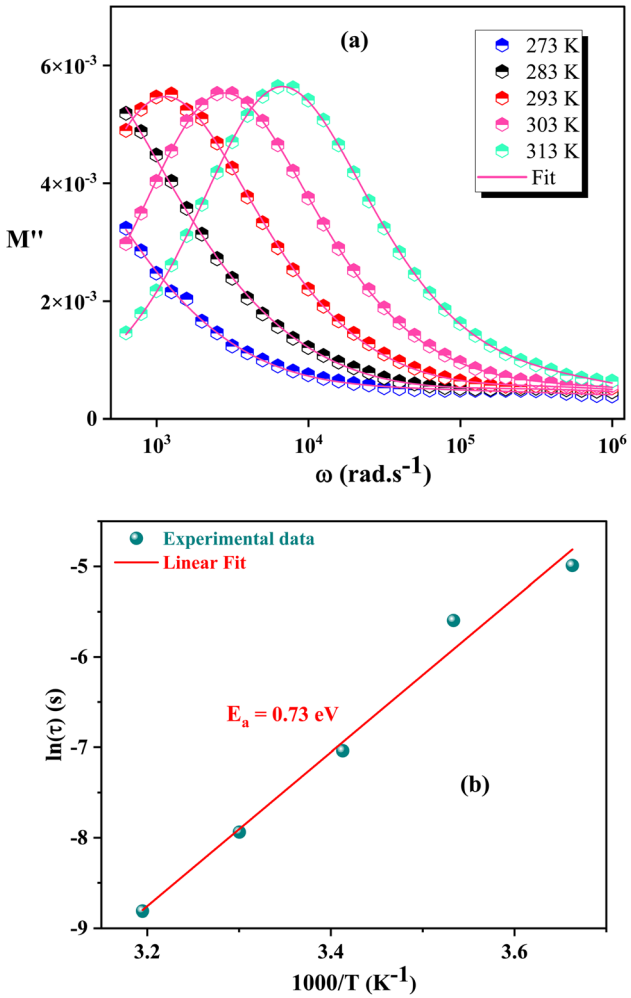

Fig. 16 (a) Angular frequency dependence of the imaginary part (M'') of the electric modulus at different temperatures, (b) plot of relaxation time (τ) as a function of $1000/T^{-1}$.

The peak frequency (ω_{max}), corresponding to the transition between long-range and short-range ionic mobility, allows the determination of the relaxation time (τ). This transition is governed by the relationship $\omega_{max}\, x\, \tau = 1$, where τ denotes the most probable relaxation time of the ions. The plot of $\ln(\tau)$ *versus* $(1000/T^{-1})$ is presented in the Fig. 16b. The activation energy of the charge carriers can be estimated using the Arrhenius law:[65]

$$\tau = \tau_0 \exp\left(-\frac{E_a}{k_B T}\right) \quad (9)$$

Here, τ_0, E_a, T, k_B, represent the relaxation time at infinite temperature, the activation energy, the measurement temperature and the Boltzmann constant respectively.

From the slope of $\ln(\tau)$ *versus* $1000/T^{-1}$ plot, the activation energy was determined to be 0.73 eV, which is consistent with the value obtained from the slope of $\ln(\sigma_{DC}\, T)$ *versus* $1000/T^{-1}$. This agreement confirms that the conduction mechanism is governed by a hopping transport.[66]

4. Conclusions

The bis(triethylammonium) chlorocuprate(II) hybrid perovskite was successfully synthesized by a slow evaporation method at room temperature. Various characterization techniques were employed to investigate the structural, optical, and electrical properties of the compound. Powder X-ray diffraction analysis confirmed that the compound crystallizes in the monoclinic system with the centrosymmetric $P2_1/c$ space group. Raman spectroscopy at room temperature, allowed the identification of the different vibrational modes and the structural composition of the crystal. The UV-Visible spectrum revealed strong optical absorption and pronounced semiconducting behavior, with the direct band gap estimated to be approximately 2.36 eV using the Kubelka–Munk function. Electrical conductivity measurements confirmed the semiconducting nature of the material. Moreover, the charge transport behavior was found to be consistent with the Correlated Barrier Hopping (CBH) model, as evidenced by the temperature-dependent variation of the frequency exponent s. These findings highlight the potential of $[(C_2H_5)_3NH]_2CuCl_4$ as a promising candidate for future optoelectronic device applications.

Conflicts of interest

There are no conflicts of interest among the authors.

Data availability

The authors confirm that the data used to support the findings of this study are included within the article and are available from the corresponding author upon reasonable request.

References

1 X. Li, *et al.*, Lead-Free Halide Perovskites for Light Emission: Recent Advances and Perspectives, *Adv. Sci.*, 2021, **8**(4), 2003334, DOI: 10.1002/advs.202003334.
2 F. Yan, S. T. Tan, X. Li, H. V. Demir, *et al.*, Light Generation in Lead Halide Perovskite Nanocrystals, *Small*, 2019, **15**(47), 1902079, DOI: 10.1002/smll.201902079.
3 D. Lencer, M. Salinga, M. Wuttig, *et al.*, Design Rules for Phase-Change Materials in Data Storage Applications, *Adv. Mater.*, 2011, **23**(18), 2030–2058, DOI: 10.1002/adma.201004255.
4 B. Champagne, A. Plaquet, J.-L. Pozzo, V. Rodriguez, F. Castet, *et al.*, Nonlinear Optical Molecular Switches as Selective Cation Sensors, *J. Am. Chem. Soc.*, 2012, **134**(19), 8101–8103, DOI: 10.1021/ja302395f.
5 F. Hao, C. C. Stoumpos, R. P. H. Chang, M. G. Kanatzidis, *et al.*, Anomalous Band Gap Behavior in Mixed Sn and Pb Perovskites Enables Broadening of Absorption Spectrum in Solar Cells, *J. Am. Chem. Soc.*, 2014, **136**(22), 8094–8099, DOI: 10.1021/ja5033259.
6 I. C. Smith, E. T. Hoke, D. Solis-Ibarra, M. D. McGehee, H. I. Karunadasa, *et al.*, A Layered Hybrid Perovskite Solar-Cell Absorber with Enhanced Moisture Stability, *Angew.*

Chem., Int. Ed., 2014, **53**(42), 11232–11235, DOI: 10.1002/anie.201406466.

7 F. Hao, C. C. Stoumpos, D. H. Cao, R. P. H. Chang, M. G. Kanatzidis, *et al.*, Lead-free solid-state organic–inorganic halide perovskite solar cells, *Nat. Photonics*, 2014, **8**(6), 489–494, DOI: 10.1038/nphoton.2014.82.

8 D. B. Mitzi, Synthesis, Structure, and Properties of Organic-Inorganic Perovskites and Related Materials, in *Progress in Inorganic Chemistry*, ed. K. D. Karlin, Wiley, 1st edn, vol. 48, 1999, pp. 1–121, DOI: 10.1002/9780470166499.ch1.

9 H. Zhu, *et al.*, Lead halide perovskite nanowire lasers with low lasing thresholds and high-quality factors, *Nat. Mater.*, 2015, **14**(6), 636–642, DOI: 10.1038/nmat4271.

10 P. Priyadarshini, S. Senapati, R. Naik, *et al.*, Lead-free organic inorganic hybrid halide perovskites: An emerging candidate for bifunctional applications, *Renewable Sustainable Energy Rev.*, 2023, **186**, 113649, DOI: 10.1016/j.rser.2023.113649.

11 K. Sahoo, *et al.*, Highly stable and luminescent formamidinium-based perovskite nanocrystal probe for temperature and mercury sensors and in vitro imaging in live cells, *J. Mater. Chem. C*, 2024, **12**(42), 17315–17327, DOI: 10.1039/D4TC02282C.

12 K. Sahoo, L. Juneja, R. Naik, S. Bhaumik, *et al.*, Double-encapsulated red-emitting formamidinium lead halide perovskite nanocrystals for fluorescence sensing and lighting applications, *Nanoscale Adv.*, 2025, **7**(17), 5411–5420, DOI: 10.1039/D5NA00412H.

13 M. Chański, A. Białońska, R. Jakubas, A. Piecha-Bisiorek, *et al.*, Structural characterization and properties of bis (1,4-H2-1,2,4-triazolium) pentachlorobismuthate (III) and cocrystal of ammonium chloride with tris (1,4-H2-1,2,4-triazolium) hexachlorobismuthate (III), *Polyhedron*, 2014, **71**, 69–74, DOI: 10.1016/j.poly.2013.12.038.

14 S. González-Carrero, R. E. Galian, J. Pérez-Prieto, *et al.*, Organometal Halide Perovskites: Bulk Low-Dimension Materials and Nanoparticles, *Part. Part. Syst. Charact.*, 2015, **32**(7), 709–720, DOI: 10.1002/ppsc.201400214.

15 S. K. Abdel-Aal, G. Kocher-Oberlehner, A. Ionov, R. N. Mozhchil, *et al.*, Effect of organic chain length on structure, electronic composition, lattice potential energy, and optical properties of 2D hybrid perovskites $[(NH_3)(CH_2)_n(NH_3)]CuCl_4$, n = 2–9, *Appl. Phys. A*, 2017, **123**(8), 531, DOI: 10.1007/s00339-017-1150-8.

16 Z.-K. Tan, *et al.*, Bright light-emitting diodes based on organometal halide perovskite, *Nat. Nanotechnol.*, 2014, **9**(9), 687–692, DOI: 10.1038/nnano.2014.149.

17 P. Gao, M. Grätzel, M. K. Nazeeruddin, *et al.*, Organohalide lead perovskites for photovoltaic applications, *Energy Environ. Sci.*, 2014, **7**(8), 2448–2463, DOI: 10.1039/C4EE00942H.

18 Z. Xu, *et al.*, Optimizing optoelectronic performances by controlling halide compositions of $MAPb(Cl_x\ I_{1-x})_3$ single crystals, *CrystEngComm*, 2019, **21**(28), 4169–4174, DOI: 10.1039/C9CE00538B.

19 Z. Lian, *et al.*, Perovskite $CH_3\ NH_3\ PbI_3$ (Cl) Single Crystals: Rapid Solution Growth, Unparalleled Crystalline Quality, and Low Trap Density toward 10^8 cm^{-3}, *J. Am. Chem. Soc.*, 2016, **138**(30), 9409–9412, DOI: 10.1021/jacs.6b05683.

20 Y. Jiang, M. A. Green, R. Sheng, A. Ho-Baillie, *et al.*, Room temperature optical properties of organic–inorganic lead halide perovskites, *Sol. Energy Mater. Sol. Cells*, 2015, **137**, 253–257, DOI: 10.1016/j.solmat.2015.02.017.

21 N. J. Jeon, J. H. Noh, Y. C. Kim, W. S. Yang, S. Ryu, S. I. Seok, *et al.*, Solvent engineering for high-performance inorganic–organic hybrid perovskite solar cells, *Nat. Mater.*, 2014, **13**(9), 897–903, DOI: 10.1038/nmat4014.

22 A. Kaiba, *et al.*, Synthesis, structural and Raman spectroscopic in organic−inorganic halide perovskites based on β-Alanine, *J. Mol. Struct.*, 2020, **1204**, 127380, DOI: 10.1016/j.molstruc.2019.127380.

23 P. Zolfaghari, G. A. De Wijs, R. A. De Groot, *et al.*, The electronic structure of organic–inorganic hybrid compounds: $(NH_4)_2\ CuCl_4$, $(CH_3NH_3)_2\ CuCl_4$ and $(C_2H_5NH_3)_2CuCl_4$, *J. Phys.: Condens. Matter*, 2013, **25**(29), 295502, DOI: 10.1088/0953-8984/25/29/295502.

24 D. Cortecchia, *et al.*, Lead-Free MA2 CuCl *x* Br 4– *x* Hybrid Perovskites, *Inorg. Chem.*, 2016, **55**(3), 1044–1052, DOI: 10.1021/acs.inorgchem.5b01896.

25 S. K. Abdel-Aal, A. S. Abdel-Rahman, *et al.*, Fascinating Physical Properties of 2D Hybrid Perovskite [(NH3)(CH2)7(NH3)]CuClxBr4−x, x = 0, 2 and 4, *J. Electron. Mater.*, 2019, **48**(3), 1686–1693, DOI: 10.1007/s11664-018-06916-7.

26 J. Li, R. Matheu, F. Ke, Z. Liu, Y. Lin, H. I. Karunadasa, *et al.*, Mosaic CuI −CuII −InIII 2D Perovskites: Pressure-Dependence of the Intervalence Charge Transfer and a Mechanochemical Alloying Method, *Angew. Chem., Int. Ed.*, 2023, **62**(20), e202300957, DOI: 10.1002/anie.202300957.

27 K. Ozga, A. O. Fedorchuk and et G. Lakshminarayana, Light operated electrooptical materials based on the [(C2H5)3NH]2CuCl4/polymer nanocomposites, *J. Mater. Sci.: Mater. Electron.*, 2014, **25**(3), 1460–1465, DOI: 10.1007/s10854-014-1752-2.

28 X. Wang, T. Zhang, Y. Lou, Y. Zhao, *et al.*, All-inorganic lead-free perovskites for optoelectronic applications, *Mater. Chem. Front.*, 2019, **3**(3), 365–375, DOI: 10.1039/C8QM00611C.

29 S. K. Wolff, D. J. Grimwood, J. J. McKinnon, D. Jayatilaka and M. A. Spackman, *Crystal Explorer*, University of Western Australia, Perth, Australia, 2007.

30 I. Soudani, K. Ben Brahim, A. Oueslati, H. Slimi, A. Aydi, K. Khirouni, *et al.*, Investigation of structural, morphological, and transport properties of a multifunctional Li-ferrite compound, *RSC Adv.*, 2022, **12**(29), 18697–18708, DOI: 10.1039/D2RA02757G.

31 A. Jezzini, A. Davidson, T. Hamieh, J. Toufaily, *et al.*, Exploring Reduced Graphene Oxide Sheets Stabilized by Cu (II) and Cu(I) Cations in Ethanol, *Crystals*, 2024, **14**(7), 654, DOI: 10.3390/cryst14070654.

32 S. Das, S. Senapati, G. K. Pradhan, S. Varadharajanperumal, R. Naik, *et al.*, A Facile Microwave-Assisted Nanoflower-to-Nanosphere Morphology Tuning of CuSe 1− x Te 1+ x for Optoelectronic and Dielectric Applications, *ACS Appl. Nano*

Mater., 2023, **6**(7), 5298–5312, DOI: 10.1021/acsanm.2c05429.

33 P. Priyadarshini, S. Senapati, S. Bisoyi, S. Samal, R. Naik, *et al.*, Zn doping induced optimization of optical and dielectric characteristics of CuInSe2 nanosheets for optoelectronic device applications, *J. Alloys Compd.*, 2023, **945**, 169222, DOI: 10.1016/j.jallcom.2023.169222.

34 C. Jelsch, K. Ejsmont and L. Huder, The enrichment ratio of atomic contacts in crystals, an indicator derived from the Hirshfeld surface analysis, *IUCrJ*, 2014, **1**, 119–128, DOI: 10.1107/S2052252514003327.

35 J. Lamotte-Brasseur, L. Dupont, O. Dideberg, *et al.*, Structure cristalline du tetracuprichlorure de triethylammonium [(C\Sb2H\Sb5)\Sb3.NH]\Sb2CuCl\Sb4, *Acta Crystallogr., Sect. B*, 1973, **29**(2), 241–246, DOI: 10.1107/S056774087300227X.

36 B. Bednarska-Bolek, Z. Ciunik, R. Jakubas, G. Bator, P. Ciapała, *et al.*, Structure and phase transitions in chloroantimonate(V) crystals: [(C2H5)3NH]SbCl6 and [(C2H5)3NH]SbCl6·1/2[(C2H5)3NH]Cl, *J. Phys. Chem. Solids*, 2002, **63**(3), 507–518, DOI: 10.1016/S0022-3697(01)00189-5.

37 I. Chaabane, W. Rekik, M. Zaghrioui, J. Lhoste, A. Oueslati, M. Gargouri, *et al.*, Synthesis, crystal structure, and ionic conductivity of a new organic–inorganic bromides (C6H9N2)2[SbBr4]Br, *Ionics*, 2024, **30**(9), 5827–5844, DOI: 10.1007/s11581-024-05680-5.

38 I. Dakhlaoui, K. Karoui, F. Hajlaoui, N. Audebrand, T. Roisnel, F. Jomni, *et al.*, [(CH3)3N(CH2)2Br]2[CoBr4] halogenometallate complex: crystal structure, high-temperature reversible phase transition, electrical and optical properties, *J. Mol. Struct.*, 2021, **1231**, 129684, DOI: 10.1016/j.molstruc.2020.129684.

39 X. Wei, *et al.*, Synthesis, crystal structure, thermal stability, and photovoltaic properties of organic-inorganic hybridized copper-based perovskite single crystals modulated by organics, *J. Mol. Struct.*, 2024, **1304**, 137634, DOI: 10.1016/j.molstruc.2024.137634.

40 M. Gassara, N. H. Hemasiri, S. Kazim, F. Costantino, H. Naïli, S. Ahmad, *et al.*, Uncovering the Role of Electronic Doping in Lead-free Perovskite (CH3 NH3)2 CuCl 4- *x* Br *x* and Solar Cells Fabrication, *ChemSusChem*, 2023, **16**(11), e202202313, DOI: 10.1002/cssc.202202313.

41 X. Wei, *et al.*, Band Gap Engineering Based on X-Site Ion Tuning in Copper Organic–Inorganic Hybrid Perovskite, *Inorg. Chem.*, 2025, **64**(32), 16495–16503, DOI: 10.1021/acs.inorgchem.5c01884.

42 I. A. Akimov, *et al.*, Orientation of electron spins in hybrid ferromagnet–semiconductor nanostructures, *Phys. Status Solidi B*, 2014, **251**(9), 1663–1672, DOI: 10.1002/pssb.201350236.

43 R. Naik, C. Kumar, R. Ganesan, K. S. Sangunni, *et al.*, Effect of Te addition on the optical properties of As2S3 thin film, *Mater. Chem. Phys.*, 2011, **130**(1–2), 750–754, DOI: 10.1016/j.matchemphys.2011.07.062.

44 W. Hallab, *et al.*, Comprehensive exploration of a two-dimensional Cu(II)-based perovskite: a high UV–Vis–NIR absorber, *J. Mater. Sci.: Mater. Electron.*, 2025, **36**(5), 349, DOI: 10.1007/s10854-025-14385-y.

45 A. Saidi, A. Mabrouki, R. Dhahri, E. Dhahri, K. Khirouni, B. F. O. Costa, *et al.*, Electronic, electrical and thermoelectric properties of Ba0.95Ca0.05Ti0.95Y0.05O2.975 compound: Experimental study and DFT-mBJ calculation, *Heliyon*, 2023, **9**(8), e18780, DOI: 10.1016/j.heliyon.2023.e18780.

46 I. Kammoun, M. Belhouchet, A. Ben Ahmed, J. Lhoste, M. Gargouri, *et al.*, Investigation of structural, optical and electrical conductivity of a new organic inorganic bromide: [C12 H17 N2]2 ZnBr4, *RSC Adv.*, 2023, **13**(12), 8034–8042, DOI: 10.1039/D3RA00561E.

47 I. Gharbi, A. Ghoudi, N. Weslati, M. Tliha, A. Oueslati, *et al*, Comprehensive study of the structural, microstructural, and electrical properties of RbZnPO4 : insights into conduction mechanisms and the OLPT models, *Mater. Adv.*, 2025, **6**(18), 6358–6369, DOI: 10.1039/D5MA00506J.

48 A. Kumar, V. Saraswat, A. Dahshan, H. I. Elsaeedy, N. Mehta, *et al.*, Exploring dielectric and AC conduction characteristics in elemental selenium glass modified with silver halides, *RSC Adv.*, 2024, **14**(29), 20933–20950, DOI: 10.1039/D4RA02999B.

49 J. R. Macdonald and W. B. Johnson, Fundamentals of Impedance Spectroscopy, *Impedance Spectrosc.*, 2005, 1–26, DOI: 10.1002/0471716243.ch1.

50 Y. Pu, Z. Dong, P. Zhang, Y. Wu, J. Zhao and Y. Luo, Dielectric, complex impedance and electrical conductivity studies of the multiferroic Sr2FeSi2O7-crystallized glassceramics, *J. Alloys Compd.*, 2016, **672**, 64–71, DOI: 10.1016/j.jallcom.2016.02.137.

51 M. Abbassi, R. Ternane, I. Sobrados, A. Madani, M. TrabelsiAyadi and J. Sanz, Ionic conductivity of apatite-type solid electrolyte ceramics Ca2ÿxBaxLa4Bi4(SiO4)6O2 (0 <x < 2), *Ceram. Int.*, 2013, **39**(8), 9215–9221, DOI: 10.1016/j.ceramint.2013.05.026.

52 M. M. Fangary, M. A. O. Ahmed, *et al.*, The influence of frequency and temperature on the AC-conductivity in TlInTe semiconductor single crystal, *Sci. Rep.*, 2025, **15**(1), 5162, DOI: 10.1038/s41598-025-87788-w.

53 S. Das, R. C. Sahoo, S. Mishra, D. Bhattacharya, T. K. Nath, *et al.*, Effects of Ni doping at Co-site on dielectric, impedance spectroscopy and AC-conductivity in La2CoMnO6 double perovskites, *Appl. Phys. A*, 2022, **128**(4), 354, DOI: 10.1007/s00339-022-05489-x.

54 S. Sidaoui, *et al.*, Crystal structure, thermal behavior and electric properties of a new semiconductor cobalt-based hybrid material, *J. Mol. Struct.*, 2023, **1294**, 136394, DOI: 10.1016/j.molstruc.2023.136394.

55 K. Moualhi, Y. Moualhi, M. Zouaoui, *et al.*, Investigation of conduction mechanisms and permittivity–conductivity correlation in a Gd-based perovskite structure, *RSC Adv.*, 2024, **14**(6), 4142–4152, DOI: 10.1039/D3RA08703D.

56 W. Ncib, A. Ben Jazia Kharrat, M. Saadi, K. Khirouni, N. Chniba-Boudjada, W. Boujelben, *et al.*, Structural, AC conductivity, conduction mechanism and dielectric properties of La0.62Eu0.05Ba0.33Mn0.85Fe0.15O3 ceramic

compound, *J. Mater. Sci. Mater. Electron.*, 2019, **30**(20), 18391–18404, DOI: 10.1007/s10854-019-02193-0.

57 A. A. Alnafea, N. Chakchouk, H. Siddiq, S. M. Altarifi, M. H. Dhaou, A. B. Rhaiem, *et al.*, Study of Alternative Current Conduction Mechanisms on the α-LiFeO2 -Based Cathode Materials, *Appl. Organomet. Chem.*, 2025, **39**(4), e70088, DOI: 10.1002/aoc.70088.

58 K. S. Rao, P. M. Krishna, D. M. Prasad, J. H. Lee and J. S. Kim, *J. Alloy. Compd.*, 2008, **464**, 497–507, DOI: 10.1016/j.jallcom.2013.03.123.

59 G. E. Pike, ac Conductivity of Scandium Oxide and a New Hopping Model for Conductivity, *Phys. Rev. B*, 1972, **6**(4), 1572–1580, DOI: 10.1103/PhysRevB.6.1572.

60 R. Das, R. N. P. Choudhary, *et al.*, Studies of structural, dielectric relaxation and impedance spectroscopy of lead-free double perovskite: Dy2NiMnO6, *J. Mater. Sci. Mater. Electron.*, 2018, **29**(22), 19099–19110, DOI: 10.1007/s10854-018-0036-7.

61 I. Soudani, *et al.*, Research on the physical properties of LiMn0.5 Fe2 O4 spinel ferrites by the combination of optical, magnetic, and dielectric behaviors, *RSC Adv.*, 2023, **13**(14), 9260–9272, DOI: 10.1039/D3RA00985H.

62 M. A. Afifi, N. A. Hegab and A. E. Bekheat, Effect of annealing on structure and electrical conductivity of evaporated indium telluride, *Vacuum*, 1995, **46**, 335–339, DOI: 10.1002/pssa.2211150216.

63 P. S. Anantha and K. Hariharan, ac Conductivity analysis and dielectric relaxation behaviour of NaNO3–Al2O3 composites, *Mater. Sci. Eng., B*, 2005, **121**, 12–19.

64 S. Chkoundali, I. Garoui, W. Trigui and A. Oueslati, Crystal structure, Hirshfeld surface analysis, conduction mechanism and electrical modulus study of the new organic–inorganic compound [C8 H10 NO]2 HgBr4, *RSC Adv.*, 2024, **14**, 8971–8980, DOI: 10.1039/D4RA00689E.

65 Y. D. Kolekar, L. J. Sanchez and C. V. Ramana, Dielectric relaxations and alternating current conductivity in manganese substituted cobalt ferrite, *J. Appl.Phys.*, 2014, **115**, 144106, DOI: 10.1016/j.jpcs.2016.03.015.

66 S. Mollah, K. K. Som, K. Bose and B. K. Chaudhuri, ac conductivity in Bi4Sr3Ca3Cu y O x (y= 0–5) and Bi4Sr3Ca3-z Li z Cu4O x (z= 0.1–1.0) semiconducting oxide glasses, *J. Appl. Phys.*, 1993, **74**, 931–937, DOI: 10.1063/1.355328.